Research Article Vol. 30, No. 15 / 18 Jul 2022 / *Optics Express* 26396

Optics EXPRESS

Depth random-access two-photon Bessel light-sheet imaging in brain tissue

DONGLI XU,[1,2] JUN B. DING,[2,3] AND LEILEI PENG[1,4]

[1] *College of Optical Science, The University of Arizona, Tucson, AZ 85721, USA*
[2] *Department of Neurosurgery, Department of Neurology and Neurological Sciences, Wu-Tsai Neuroscience Institute, Stanford University, Stanford, CA 94305, USA*
[3] *dingjun@stanford.edu*
[4] *lpeng@optics.arizona.edu*

Abstract: Two-photon light-sheet fluorescence microscopy enables high-resolution imaging of neural activity in brain tissue at a high frame rate. Traditionally, light-sheet microscopy builds up a 3D stack by multiple depth scans with uniform spatial intervals, which substantially limits the volumetric imaging speed. Here, we introduce the depth random-access light-sheet microscopy, allowing rapid switching scanning depth for light-sheet imaging. With a low-cost electrically tunable lens and minimum modification of an existing two-photon light-sheet imaging instrument, we demonstrated fast random depth hopping light-sheet imaging at 100 frames per second in the live brain slice. Through depth random-access, calcium activities for an astrocyte were recorded on four user-selected detection planes at a refreshing rate of 25 Hz.

1. Introduction

Two-photon microscopy (TPM) provided an efficient way to deliver photons into the brain tissue, thus allowing high spatial resolution imaging in deep tissue with a decent signal-to-noise ratio (SNR). Raster scanning TPM has been the standard tool for 3D deep tissue imaging, albeit using a slow sequential voxel scanning strategy [1]. Although the imaging speed can be improved by adopting faster beam scanning approaches, speedier scanning also means a shorter pixel dwell time and lower SNR. The SNR loss could only be compensated by increasing the excitation power, which increases the rate of photobleaching and the chance of photodamage for biological specimens.

To achieve a high imaging speed while maintaining the SNR, projection imaging techniques employ an extended excitation beam to scan 2D projection images of sparsely labeled samples, then reconstruct 3D locations of activities with the post-processing algorithm [2–5]. Meanwhile, random-access scanning two-photon imaging, which exploits fast laser point scanners, enables selective access to targeted regions, thus significantly increasing the imaging speed without lowering the pixel dwell time [6–8]. Various multi-foci scanning methods [9–13] and whole-field temporal focusing methods [14] took parallelization as a strategy to improve the acquisition throughput. Two-photon light-sheet microscopy (TPLSM) [15] emerges as a faster 3D imaging method in comparison to the traditional point scanning TPM. TPLSM gains the intrinsic 3D resolving ability by decoupling the excitation and the detection, confining its excitation within the layer of interest, therefore minimalizing photon bleaching and allowing the use of a camera to acquire 3D imaging. TPLSM with Bessel beam excitation can further extend the excitation penetration depth in the scattering tissue [16–18]. The imaging frame rate of the TPLSM is accelerated by the modern high-speed scientific camera. However, the volumetric imaging rate is still limited by the speed of the depth scanning mechanism. With faster focal depth scanning methods, such as Oblique-plane microscopy (OPM) [19,20], swept confocally-aligned planar excitation (SCAPE) microscopy [21], and other single objective light-sheet microscopes [22–24] achieved rapid volumetric imaging at the cost of lowering image SNR. These methods are less

#456871 https://doi.org/10.1364/OE.456871
Journal © 2022 Received 22 Feb 2022; revised 27 May 2022; accepted 7 Jun 2022; published 7 Jul 2022

ideal in the case of TPLSM because two-photon imaging has a lower excitation rate and requires longer dwell time to achieve a decent SNR. Because of its low cost, Electrically Tunable Lens (ETL) is widely used as a remote focusing approach in rapid 3D light-sheet microscopy [25], despite its existing limitations. For example, ETL is not the fastest tunable device available and has highly variable performances under different driving conditions.

Our work aims to develop a depth random-access TPLSM, which allows selective imaging layers of interest within a tissue volume. We expect depth random-access TPLSM to achieve a faster 3D refreshing rate than existing TPLSM without sacrificing the exposure time per image layer, in a way that is similar to how random-access point scanning TPM performs at a higher imaging speed than raster scanning TPM. The challenge in depth random-access TPLSM is the lack of high-speed focus switching devices. Point random-access TPM relies on fast switching optical scanners, for example, acoustic optical deflectors. Focal depth scanners, especially those can support the field of view of TPLSM, have much slower switching speeds and are more suitable for repeated periodic scans. Here, we present a depth random-access TPLSM method that is built on a low-cost slow focal depth scanner and yet capable of selective acquiring optical sections at desired depths. The method does not require a significant change of the optics in an existing TPLSM. We implemented the depth random-access on an existing two-photon Bessel beam light-sheet microscope [16,26] equipped with an ETL, which works as a detection focal depth scanning device. With the ETL-based focal depth random-access, we demonstrated 100 Hz TPLSM imaging at user-selected depths. With the depth random-access TPLSM, we performed calcium imaging on a live mouse brain slice over four arbitrarily chosen depths at a refreshing rate of 25 Hz.

2. Methods

2.1. Depth random-access two-photon Bessel light-sheet imaging

The Bessel two-photon light-sheet microscope [Fig. 1(a)] consists of an excitation path and a detection path that meet each other at a 90-degree angle. In the excitation path, a 920 nm laser beam from a Ti-sapphire laser (Maitai HDPS, Spectra-physics, 80 MHz repetition rate, 1.5 W maximal output) is directed through a Pockels cell (Model 350-80, Conoptics). The Pockels cell works as a high-speed laser shutter and an illumination intensity controller that tunes the excitation power on the sample. It operates at two shutter modes: during imaging, it performs 3-4ms long exposures for light-sheet scanning with precise timing, which is essential for random access; during system testing and calibration, it enables 200-µs snapshots of the laser beam to measure and verify performance. The beam passes through a set of beam expander and an axicon lens (AX251-B, Thorlabs), which shapes the Gaussian laser beam into a Bessel beam. The Bessel beam is then projected onto a galvo scanner pair. An x-galvo scanner (6215H, Cambridge Technology) creates the illumination light-sheet, and a z-galvo scanner (GVS001, Thorlabs) controls the depth of the light-sheet. The scanning light-sheet is then sent into a 28.6x illumination objective (0.66 NA, 54-10-7, Special Optics) through a pair of 4f-relay lenses. On the detection path, a 40x water-immersion detection lens (NA 0.8, LUMPLFLN40XW, Olympus) is used to collect the fluorescence signals. An ETL (EL-10-30-Ci-VIS-LD, Optotune) driven by a sinusoidal current signal is optically conjugated to the back focal plane of the detection objective through a pair of 4f relay lenses. The design allows the ETL to dynamically tune the position of the detection plane without magnification change [25]. The fluorescence image is captured by a camera (C13440-20CU, Hamamatsu).

In our system, the ETL is placed at the conjugate back focal plane of the detection objective and continuously driven by a 50 Hz sinusoidal wave, thus propelling the detection focal plane to shift periodically. To maintain the coupling status of the excitation laser and the detection focus plane during light-sheet imaging, the z-galvo scanner moves the excitation Bessel beam to track the detection focal plane by using a driving waveform calibrated to the ETL scan [Fig. 1(b)].

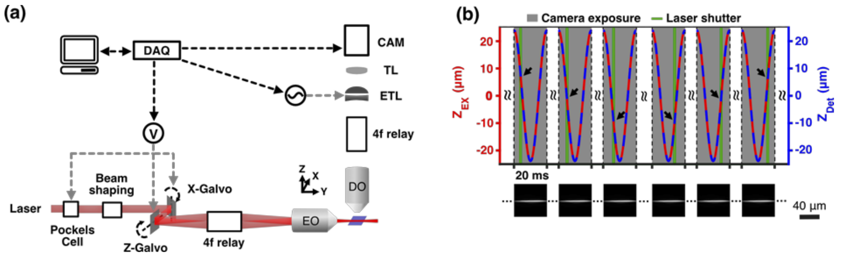

Fig. 1. Depth random-access two-photon light-sheet microscope. (a) The two-photon Bessel beam light-sheet microscope includes a beam shaper to convert the Gaussian excitation laser (in red) into a Bessel beam, a Pockels cell acting as the laser shutter, two galvo scanners, and a camera. The ETL on the detection arm is driven by a 50 Hz sinusoidal current, which causes the detection focal plane (in blue) to travel back and forth along the depth (Z) direction. All electric components are controlled and synchronized by NI DAQ cards and a host computer. The y-direction is the excitation laser beam propagating direction, and the x is the light-sheet scanning direction. EO, excitation lens; DO, detection lens; TL, tube lens; CAM, camera. (b) Verification of the coupling between excitation beam and detection focal scanning. Top: Timing chart of the Bessel beam depth and the detection focal plane depth. The depth of the excitation Bessel beam (red dash line) is tightly coupled with the detection focal plane scan (blue dash line), making the excitation beam always in focus on the camera. To verify the coupling, the x-galvo scanner was held stationary, the camera was set to be active during linear regions of focal depth scans (grey shaded area), and the laser shutter opened briefly for 200 μs at variable timing points. The resulting image data are shown below. Bottom: Image data that verified the coupling between ETL-driven detection plane scan and the excitation beam depth. Sharp in-focus excitation beam images taken with different exposure timing points (bottom row), i.e., different focal plane depths, proved that the excitation beam depth was always synchronized with the detection focal plane.

Such a method enabled us to verify depth synchronization between ETL and z-galvo. The laser shutter (Pockels cell) was used to take snapshots of the laser beam while the laser beam and imaging focal plane move along the z direction. Image results show the laser beam was always in focus, proving its depth was well synchronized with the focal plane movement controlled by the ETL.

Depth random access imaging is achieved by a combination of camera exposure timing control and synchronized laser beam scanning. Figure 2(a) illustrates the 3D random depth imaging geometry and plots the corresponding timing diagram of controlling waveforms. The ETL is driven by a sinusoidal waveform (50 Hz with 140 mA peak to peak amplitude and 125 mA bias) in all data sets presented in this work. The depth scan was precisely calibrated (See Section 2.3, Supplementary 1 Fig. S1 and S2), which produced the signal waveform for the z-galvo scanner to track the ETL focus scanning. The camera captures an image within each of the two linear ETL scanning ranges during a single ETL scanning period, resulting in an imaging frame rate of 100 Hz. The laser exposure window overlaps with the camera exposure and typically lasts 3-4 ms. During the exposure, the x-galvo scanner sweeps the laser through the camera field of view (FOV). Meanwhile, the laser beam driven by both the x and z galvo scanners, also moves in the depth to track the focal depth change during the exposure. As a result, the light sheet is titled around the y-axis. The titling angle varies depending on the x-width of the lateral field of view and was typically 14°-19° in this work (See Supplementary 1 Table S1). The acquired image on the detection camera is an X-Y plane projection of the light-sheet plane, causing a minor isotropic sampling effect in the x-direction (less than 6% in our system). The depth of the light sheet can be electronically controlled by the exposure delay Δt_n. Varying the timing moves the imaging layer within the accessible volume, therefore changing the imaging depth. Operations of galvo scanners, ETL, laser shutter, and camera exposure are controlled by a host PC through NI DAQ cards. An in-house software written in LabVIEW is used to perform ETL calibration and imaging acquisition.

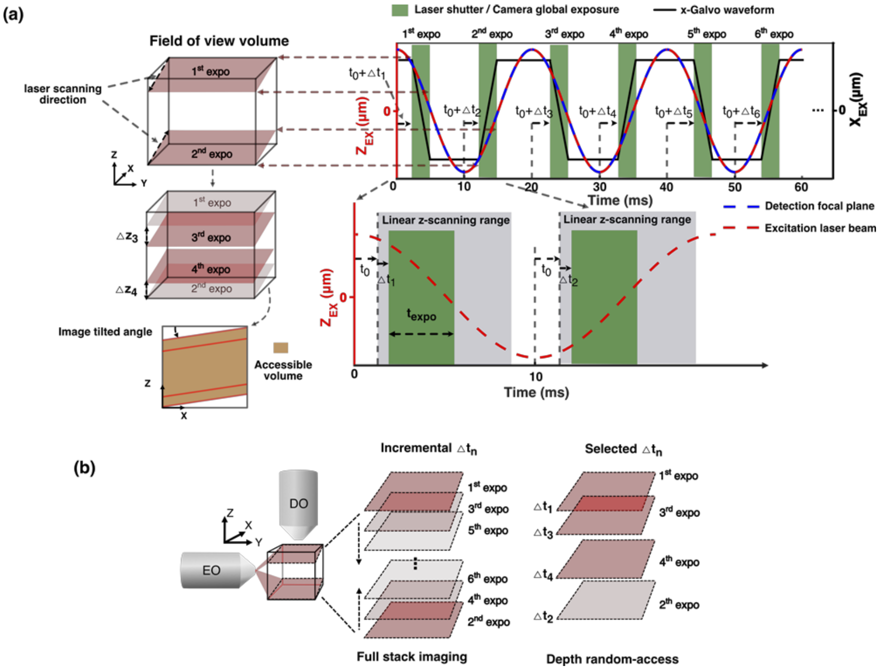

Fig. 2. Schematic of depth random-access two-photon light-sheet imaging method. (a) Left: Schematic of depth random access imaging geometry; Right: the timing plot of key imaging control signals(top) and enlarged timing plot of two consecutive exposures in a single ETL-driven cycle (bottom). The ETL is driven by a 50 Hz sinusoidal wave (blue dash line). The z-galvo scanner moves the depth of the excitation laser beam (red dash line) to maintain coupling with the focal depth of the camera. The x-galvo scanner sweeps the excitation laser beam across the imaging field of view (black line) and forms a light sheet plane (red planes in the left schematic) during the laser exposure. Imaging planes are slightly titled due to the moving focal depth during an exposure, resulting in a tilted 3D scan volume. The typical titled angles were 14°-19° (See Supplementary 1 Table S1). The camera is set to active within two linear z-scanning ranges of each ETL scanning cycle (grey shaded areas of the timing plot), within which contains the laser exposure window (green shaded areas). An initial delay t_0 is introduced to set the light sheet plane at the top (or bottom) layer of the imaging volume. An additional delay Δt individually defined for each exposure moves the exposure window to a later time in the linear z-scanning range, and therefore, move the depth of the light-sheet image toward the other end of the volume. With a known z-scanning speed v_z measured by the ETL calibration, light-sheet image's relative depth position is controlled by $\Delta z = \Delta t \times v_z$. The direction of Δz is from top to bottom in even numbered exposures and in the reverse direction in odd numbered exposures. The user can set a series of Δt_1, $\Delta t_2, \ldots$, Δt_n to selectively imaging planes in the volume. (b) Flexible imaging strategies by adopting different exposure delay Δt_n during 3D imaging. The relative depth position of each light-sheet plane image depends on its laser exposure delay time Δt_n, which can be tuned by adjusting the laser shutter controlling signal. The system can perform a full-stack 3D imaging scan with uniform spatial intervals by gradually shifting the timing of the exposure window after each exposure (incremental Δt_n), or image selective layers by using user-defined Δt_n.

The ETL scans through the field of view volume at a rate of 100 Hz, allowing random-depth access imaging at 100 FPS. As shown in Fig. 2(b), by conducting exposures with a series of incremental delay Δt_n, the system can perform 3D full-stack light-sheet scans. Alternatively, by setting individual timing Δt for each exposure, we can access any chosen layers in the imaging volume on demand.

2.2. System performance

As in all light sheet imaging systems, the FOV volume of our system is set by a combination of the camera FOV in the x-direction, length of the excitation beam (y-direction), and linear range of the ETL scanning (in the z-direction). We used a 60 µm long Bessel beam, although the system supports up to 500 µm long Bessel beam for imaging transparent tissue samples. The linear range of the ETL scanning is estimated at 57 µm. The approximate FOV volume is $x \times 60 \times 57$ μm^3 (in xyz-direction) with a variable x depends on camera settings. In this work, we typically used x-width between 70-90 µm. Our random depth imaging method scans tilted image planes within the FOV cube. Therefore, two corners of the FOV cube are not accessible. A large tilting angle would cause a significant loss of FOV volume. The tilted angle is determined by the ratio of x-galvo scan speed v_x and the depth scan speed v_z. Decreasing the exposure time can lower the x-galvo scan speed, resulting in a smaller tilted angle for the random-access light-sheet imaging, but accompanied by decreasing the exposure duty cycle, i.e., the image signal level of the system. To balance the exposure duty cycle with the size of the accessible volume, we used exposure times at 3-4 ms over 70-90 µm wide FOV, which set the tilted angle at 14° - 19° (Supplementary 1 Table S1), causing about 30% loss of FOV volume. Meanwhile, the exposure duty cycle was 3-4 ms active exposure vs. 7-6 ms idle time. The idle time is needed for the sCMOS camera to perform line-rolling readout and re-arm (See Supplementary 1 Table S1). The random-access mode does not cause a significant change in the exposure duty cycle, and therefore maintains a similar SNR performance compared to existing two-photon light-sheet systems.

In previous ETL-based light sheet systems, 3D image stacks were typically collected with multiple even-spaced fast exposures during each ETL-driven focal depth sweep [25]. In such an approach, the amplitude and frequency of the ETL driving signal need to be changed according to the stack layer numbers and volume thickness. Because the ETL's dynamic response is nonlinear and varies with the device temperature [25,27], changing the driving parameters, as discussed in the next section, requires extra warm-up time to re-stabilize the ETL and recalibration on the ETL response, which adds complexity in the instrument operation.

In our random-access method, the ETL is placed under constant driving parameters. All experiments presented here used a 50 Hz sinusoidal current with 140 mA peak to peak amplitude and 125 mA bias to drive the ETL. The driving signal of the z-galvo scanner was calculated from the ETL calibration measurement and remained unchanged in all experiments. The image frame rate is fixed at 100 Hz, twice of the ETL driving frequency. Thus, the depth access rate is limited by the scanning speed of the ETL. In our method, the depth position of each acquired light-sheet image is electronically controlled by the delay timing Δt of the individual exposure. Both imaged layer number and the location for each layer are freely adjustable without altering the ETL driving parameters. This characteristic makes our depth random access method extremely flexible for light-sheet imaging.

2.3. Calibration for the ETL dynamics

The depth random-access light-sheet imaging method requires a precise matching between the laser beam depth (Z_{EX}) and the ETL-modulated focal plane (Z_{Det}). As demonstrated by previous works in fast ETL-driven light-sheet imaging, the dynamic behavior of the ETL under a sinusoidal current signal is variable depending on the driving signals and device temperature [25,27]. The depth of focus (DOF) of the NA 0.8 emission detection lens in the system is approximately

1 µm, and the Bessel beam we used in this study had a 1.1 µm width and a length of 60 µm. To achieve reliable depth random-access imaging, our method requires a stable ETL dynamic response and an excitation beam depth that matches the ETL-driven focus depth at an accuracy better than 1 µm. Hence, we developed an ETL calibration method to measure ETL-driven depth scanning behavior and establish preparation protocols for using ETL in random access scans. All measurements were taken under the same ETL driving sinusoidal waveform (50 Hz with 140 mA peak to peak amplitude and 125 mA bias), and were repeated over time under different scenarios to test the stability and repeatability of the ETL-driven depth scan. Through the stability study in the next section, we verified after sufficient warm-up under the same driving signal, the ETL's dynamics response is sufficiently stable and repeatable for daily operation and can support up to 60 µm depth scans.

With a 50 Hz sinusoidal driving signal applied to the ETL, the time varying detection plane depth, $Z_{Det}(t)$, is a quasi-sinusoidal function, which depends on the applied driving signal and the response characteristics of ETL. The ETL calibration aims to measure the $Z_{Det}(t)$ function and calculate a voltage driving signal of the z-galvo scanner, so that the scanner can move the excitation depth in precise synchronization with the detection plane. A 200 µM Fluorescein solution was used as the test sample during the calibration process. The laser beam was kept stationary at a depth of Z_{EX} in the imaging volume to serve as an image target with known depth. The applied 50 Hz sinusoidal waveform on the ETL propelled the detection plane across the volume periodically. The Pockels cell, acting as a fast shutter, controlled the exposure timing of the laser beam on the camera sensor with sub-millisecond accuracy. A series of image exposures were taken at different time points during these repeated scanning cycles. Among these exposures, a sharp image of the stationary beam could be seen when the detection plane was conjugated with the laser beam plane $Z_{Det}(t) = Z_{EX}$. During each cycle, $Z_{Det}(t)$ scanned twice around the entire scan depth, and two conjugation timing points were expected for each depth Z_{EX}. The conjugation timing t was obtained by examining the image contrast vs. laser shutter timing and finding the timing when a maximal contrast is reached. To extract the whole spatial trajectory $Z_{Det}(t)$, a conjugation timing series $[t_0, t_1, t_2, \ldots, t_n]$ need to be measured at $[Z_{EX,0}, Z_{EX,1}, Z_{EX,2}, \ldots, Z_{EX,n}]$. Supplement 1 Fig. S1 shows details of the calibration process. To identify $Z_{Det}(t)$, the excitation beam was set to 28 depth points across the imaging volume in a 1.6 µm step size. At each depth, the timing of $Z_{Det}(t) = Z_{EX}$ was measured with 200 µs accuracy. Results of calibration measurements were fitted with a 6-degree polynomial function. The fitted curve $Z_{Det}(t)$ was used to drive the z-galvo scanner in imaging experiments. The resulting fitted curve $Z_{Det}(t)$ is valid for the specific ETL driving waveform. If the ETL driving waveform changes in frequency, amplitude or bias, re-calibration will be needed.

2.4. Temporal stability of the ETL

We performed ETL stability testing in three scenarios that mimicked different experiment conditions: cold-start, warm-start, and hot-start [Supplement 1 Fig. S2(a)]. The cold-start test aimed to measure the warm-up time for the ETL to reach a stable response after an overnight rest. The warm-start test mimicked situations after a pause of imaging experiments and measured the recovering time the ETL needs after a 5 minutes pause from continuous depth scans. The hot-start test reduced the pause time to 2 minutes and measured the re-stabilizing time after a brief pause. During each testing, calibration measurements were repeated 100 times, and the last measurement $Z_{Det,100}(t)$ was recorded as the stabilized ETL response. The mean difference between the prior 99 calibration measurements and the stabilized ETL response, Z, were used to quantify ETLs stability over All tests were performed at room temperature of 22 °C.

Supplement 1: Fig. S2(b)–(d) plots a group of test results from 10-day repeated tests. The cold-start test result [Supplement 1 Fig. S2(b)] shows the ETL re-stabilized after 60 minutes of continuous running. The mean difference dropped to 0.5 µm, which was below the depth of focus of the detection objective, indicating a one-hour daily warm-up will be sufficient. Two rounds of warm-start tests were performed after the cold start test, then followed by the hot start tests. Results [Supplement 1 Fig. S2(c)] show that the re-stabilizing time after a 5-minute pause is 30 minutes. Hot-start test results [Supplement 1 Fig. S2(d)] showed only 1 minute was needed to re-stabilize the ETL if the pause was shortened to 2 minutes. These tests show the ETL can always reach a repeatable dynamic response during daily operation, if sufficient warm-up is given to the device. Mean differences within 10-day standard measurements [Supplement 1 Fig. S2(e)] were below 0.5 µm. Through these tests, we concluded that the ETL was highly repeatable and robust device for the depth random-access light sheet method, and weekly ETL calibration would be sufficient for maintaining the proper operation of the instrument.

2.5. *Mouse brain slices live imaging*

All experiments were performed in accordance with protocols approved by the Stanford University and the University of Arizona Animal Care and Use Committee in keeping with the National Institutes of Health's Guide for the Care and Use of Laboratory Animals.

Thy1-YFP-H (JAX 003782) and Aldh1l1-cre (JAX 023748) transgenic mice were used in the imaging. Both were obtained from Jackson Lab and maintained as heterozygotes by crossing with C57BL/6J (JAX 000664). Mice are group-housed under a reverse 12 h:12 h light/dark cycle.

Viruses (rAAV5.CAG.flex.GCaMP6s; Addgene, Cat.No.100842-AAV5) were delivered to 5-week-old Aldh1l1-cre mice brains by stereotaxic injection. Briefly, mice were anesthetized with 2% isoflurane and given the analgesic buprenorphine SR (0.5 mg/kg of body weight), then head-fixed on a stereotaxic frame (Kopf instrument). A glass needle was used to deliver the virus into the mouse brain at the coordinate of AP: 1.2 mm, ML: ±2 mm from bregma, DV: -2.2 mm from the brain surface. A total of 300 nL virus solution was injected at an infusion rate of 100 nL/min. Following virus injection, the scalp was sutured, and mice were returned to their home cages for 4 weeks before imaging.

Mice were decapitated under isoflurane anesthesia, and the brains were transferred into ice-cold oxygenated (95% CO_2 and 5% O_2) artificial cerebrospinal fluid (ACSF, containing (in mM): 125 NaCl, 2.5 KCl, 1.25 NaH_2PO_4, 25 $NaHCO_3$, 1 $MgCl_2$, 2 $CaCl_2$ and 15 D(+)-Glucose). Then, 300-µm-thick coronal slices were obtained by a vibratome (Leica VT 1200S) and incubated at 34 °C in ACSF. After 30 min of recovery, the brain slices were maintained at room temperature. During imaging, slices were submerged in an imaging chamber constantly perfused with oxygenated ACSF.

Both Thy1-YPF-H and Aldh1l1-cre brain slices were imaged at 920 nm with average power up to 208 mW. The imaging depth of the 2p light-sheet imaging method depends on the scattering properties of the sample. For the live mouse brain slice, we have reported light-sheet images at 100 FPS with high imaging quality up to 100 µm into the brain tissue [26], whereas in zebrafish, we reported tissue penetration up to 500 µm [16]. We did not observe significant photobleaching or any tissue damage during imaging.

3. Results

3.1. *Thy1-YFP mouse brain slices imaging*

We demonstrated 3D light-sheet imaging using Thy1-YFP mouse brain slices. The system first performed full-stack volumetric imaging over 36 optical sections with 0.63 µm depth intervals by incrementally change the laser exposure timing of each exposure (Fig. 3 and Visualization 1 and Visualization 2). Sub-micron-wide fine structures, such as dendrites and spines, can be clearly identified in the image. The images have a 0.5 µm lateral resolution. Sections of dendrites are well aligned between image layers, proving that the excitation light-sheet was indeed tightly synchronized with the detection focal shifting. At a frame rate of 100 Hz, the system acquired the 36-layer 3D image at a volume rate of 2.8 Hz.

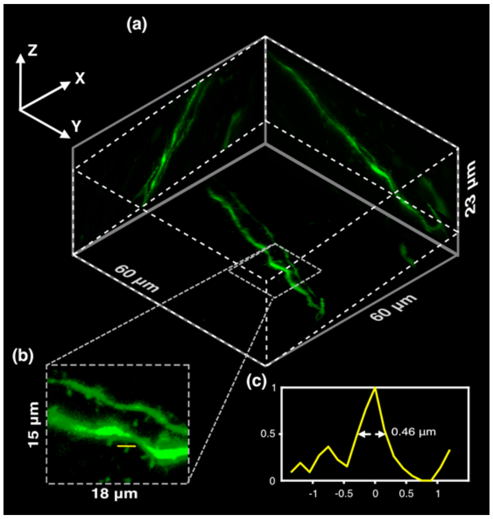

Fig. 3. Full-stack 3D two-photon light-sheet imaging with synaptic resolution in live neural tissue (detail imaging parameters are listed in Supplement 1, Table S1). A $60 \times 60 \times 23$ μm^3 volume (cropped from the original $90 \times 74.4 \times 23$ μm^3 raw dataset) of layer-5 dendrites in a Thy1-YFP-H mouse brain slice was acquired at 100 frames per second. The image set contains 36 optical sections with 0.6 µm intervals. Slice-by-slice flythrough and 3D render are available as Visualization 1 and Visualization 2. (a) Maximum intensity projection images along the X, Y and Z axis of the entire 3D dataset. (b) Zoomed-in view of a selected region. (c) Cross section plot at a spine neck with a full width half maximum of 0.46 µm, which matches the expected optical resolution.

3.2. Depth random-access Ca^{2+} imaging of an astrocyte

We also performed depth random-access Ca^{2+} imaging of GCaMP6s-labeled astrocytes in the Aldh1l1-cre mouse brain slice (Fig. 4 and Visualization 3). We compared the time-lapse full-stack dataset with the selective-layer dataset. In the full stack dataset, 500 sets of 3D stacks, each containing 51 sections with equal 0.63 µm spatial intervals, were acquired at a volume refreshing rate of 2 Hz. Fluorescence signals from spontaneous Ca^{2+} activities were observed over a duration of 2 minutes under an excitation power of 200 mW, which did not cause observable photobleaching. Spontaneous Ca^{2+} activities were seen in 3D (Visualization 3). Maximum signal levels of Ca^{2+} activities during the observation period were rendered in 3D, allowing visualizing the astrocyte structure [Fig. 4(a)]. We then performed rapid selective-layer imaging on four sections [Fig. 4(b) left] within the volume at a refreshing rate of 25 Hz. Ca^{2+} activities traces taken at 25Hz [Fig. 4(b) right] show frequent fast rising events with a typical rising time of 0.3-0.5 seconds [Fig. 4(d)], which could not be seen in traces of the same regions in the full-stack imaging results. The rising times of these events are shorter than the response speed supported by the 2Hz 51 planes depth scan imaging. These events also have a low signal level, which would fall below the noise level if the per-section exposure time is decreased. The depth random-access imaging allowed us to observe these 3D Ca^{2+} dynamics and quantify their time characteristics in live brain tissue at a faster refreshing rate and without sacrificing the signal to noise ratio.

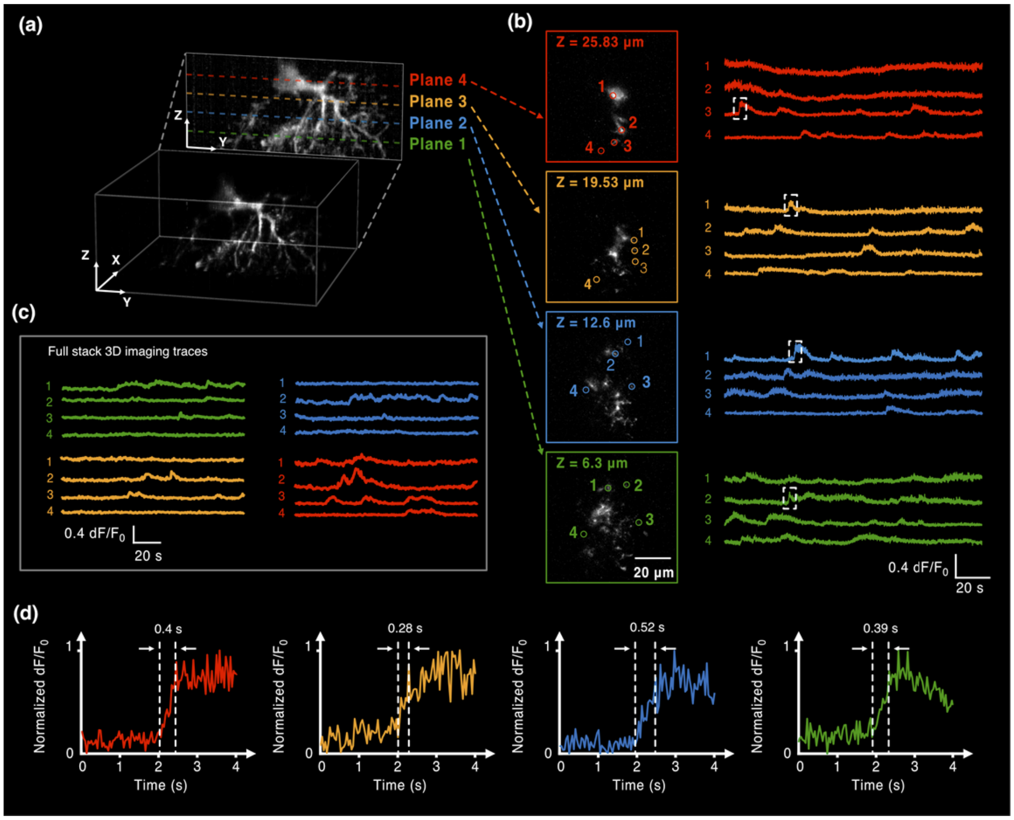

Fig. 4. Depth random-access light-sheet imaging of a GCaMP6s labeled astrocyte in the striatum of a mouse brain (detail imaging parameters are listed in Supplement 1 Table S1). (a) 3D rendering and x-direction maximum intensity projection of the astrocyte in a volume of $72 \times 72 \times 32$ μm^3. The structure dataset was reconstructed from the astrocyte Ca2+ activities over 2 minutes of 51 planes full-stack image recording at a 2 Hz refreshing rate. 3D rendered activity is available in Visualization 3. (b) Left: four selected random-accessing image planes, located at the depth of 25.83 μm, 19.53 μm, 12.6 μm and 6.3 μm in the volume. Several regions of interest (numbered circles) were selected for Ca^{2+} activity analysis. Right: Ca^{2+} activity traces in ROIs recorded at a 25 Hz refreshing rate. These traces contained frequent fast-rising events (dashed boxes). (c) Activity traces observed in the same ROIs by 51 planes full-stack recording. At a 2 Hz acquisition rate, these traces did not contain significant fast events. (d) Zoom-in views of fast-rising events marked in (b). Rising times of these events typically are less or equal to 0.5 seconds.

4. Discussion and conclusion

Traditional rapid volumetric imaging methods often compromise the imaging SNR. We present a low-cost solution to randomly access imaging planes in a light sheet system while maintaining similar exposure duty cycle, framerate and FOV. We implemented the random depth access method on an existing ETL-driven two-photon Bessel liht sheet system and demonstrated 3D time-lapse neural tissue imaging at a significantly improved refreshing rate. The faster rate allowed us to observe fast Ca^{2+} dynamics in GCaMP6s-labeled astrocytes that were not detectable at the typical 3D full-stack light-sheet imaging rate.

The depth access speed of our current implementation of this method is limited by the scanning speed of the ETL. Some applications, such as voltage imaging in neural tissue, need a minimum imaging rate of 1000 Hz, and will require a faster focal scanning method. Several devices, such as deformable mirror [28] and TAG lenses [29] are capable of faster depth scan and high volumetric rate for voltage signal imaging. Ultimately, the imaging speed is limited by the imaging SNR. For neural imaging, the 2-photon excitation light power is limited by the tissue photodamage threshold, and voltage sensors generally have much weaker signals compared to the Ca^{2+} sensors. Developments on brighter live imaging sensors are needed to support faster imaging.

Our method applies to all light sheet imaging systems using remote focal scan devices. Implementing our technique on existing light-sheet microscopes does not require hardware modification. The method provides a low-cost solution for accelerating the imaging speed in signal-limited 3D imaging applications, such as two-photon neural tissue imaging, where the signal strength is weak, but a faster 3D imaging rate is needed.

Funding. National Institute of Biomedical Imaging and Bioengineering (R01EB01548); National Science Foundation (2016035); GG Gift Fund.

Disclosures. The authors declare no competing interests.

Data availability. Data presented in this paper are available from the corresponding author upon reasonable request.

Supplemental document. See Supplement 1 for supporting content.

References

1. F. Helmchen and W. Denk, “Deep tissue two-photon microscopy,” Nat. Methods **2**(12), 932–940 (2005).
2. R. Lu, W. Sun, Y. Liang, A. Kerlin, J. Bierfeld, J. D. Seelig, D. E. Wilson, B. Scholl, B. Mohar, M. Tanimoto, M. Koyama, D. Fitzpatrick, M. B. Orger, and N. Ji, “Video-rate volumetric functional imaging of the brain at synaptic resolution,” Nat. Neurosci. **20**(4), 620–628 (2017).
3. R. Lu, Y. Liang, G. Meng, P. Zhou, K. Svoboda, L. Paninski, and N. Ji, “Rapid mesoscale volumetric imaging of neural activity with synaptic resolution,” Nat. Methods **17**(3), 291–294 (2020).
4. A. Song, A. S. Charles, S. A. Koay, J. L. Gauthier, S. Y. Thiberge, J. W. Pillow, and D. W. Tank, “Volumetric two-photon imaging of neurons using stereoscopy (vTwINS),” Nat. Methods **14**(4), 420–426 (2017).
5. Y. Yang, B. Yao, M. Lei, D. Dan, R. Li, M. V. Horn, X. Chen, Y. Li, and T. Ye, “Two-Photon Laser Scanning Stereomicroscopy for Fast Volumetric Imaging,” PLoS One **11**(12), e0168885 (2016).
6. K. M. N. S. Nadella, H. Roš, C. Baragli, V. A. Griffiths, G. Konstantinou, T. Koimtzis, G. J. Evans, P. A. Kirkby, and R. A. Silver, “Random-access scanning microscopy for 3D imaging in awake behaving animals,” Nat. Methods **13**(12), 1001–1004 (2016).
7. G. Katona, G. Szalay, P. Maak, A. Kaszas, M. Veress, D. Hillier, B. Chiovini, E. S. Vizi, B. Roska, and B. Rozsa, “Fast two-photon in vivo imaging with three-dimensional random-access scanning in large tissue volumes,” Nat. Methods **9**(2), 201–208 (2012).
8. G. Duemani Reddy, K. Kelleher, R. Fink, and P. Saggau, “Three-dimensional random access multiphoton microscopy for functional imaging of neuronal activity,” Nat. Neurosci. **11**(6), 713–720 (2008).
9. A. Cheng, J. T. Gonçalves, P. Golshani, K. Arisaka, and C. Portera-Cailliau, “Simultaneous two-photon calcium imaging at different depths with spatiotemporal multiplexing,” Nat. Methods **8**(2), 139–142 (2011).
10. J.-L. Wu, Y.-Q. Xu, J.-J. Xu, X.-M. Wei, A. C. S. Chan, A. H. L. Tang, A. K. S. Lau, B. M. F. Chung, H. Cheung Shum, E. Y. Lam, K. K. Y. Wong, and K. K. Tsia, “Ultrafast laser-scanning time-stretch imaging at visible wavelengths,” Light: Sci. Appl. **6**, e16196 (2017).
11. D. R. Beaulieu, I. G. Davison, K. Kılıç, T. G. Bifano, and J. Mertz, “Simultaneous multiplane imaging with reverberation two-photon microscopy,” Nat. Methods **17**(3), 283–286 (2020).
12. J. Wu, Y. Liang, S. Chen, C.-L. Hsu, M. Chavarha, S. W. Evans, D. Shi, M. Z. Lin, K. K. Tsia, and N. Ji, “Kilohertz two-photon fluorescence microscopy imaging of neural activity in vivo,” Nat. Methods **17**(3), 287–290 (2020).

13. J. Demas, J. Manley, F. Tejera, K. Barber, H. Kim, F. M. Traub, B. Chen, and A. Vaziri, “High-speed, cortex-wide volumetric recording of neuroactivity at cellular resolution using light beads microscopy,” Nat. Methods **18**(9), 1103–1111 (2021).
14. T. Schrödel, R. Prevedel, K. Aumayr, M. Zimmer, and A. Vaziri, “Brain-wide 3D imaging of neuronal activity in Caenorhabditis elegans with sculpted light,” Nat. Methods **10**(10), 1013–1020 (2013).
15. T. V. Truong, W. Supatto, D. S. Koos, J. M. Choi, and S. E. Fraser, “Deep and fast live imaging with two-photon scanned light-sheet microscopy,” Nat. Methods **8**(9), 757–760 (2011).
16. M. Zhao, H. Zhang, Y. Li, A. Ashok, R. Liang, W. Zhou, and L. Peng, “Cellular imaging of deep organ using two-photon Bessel light-sheet nonlinear structured illumination microscopy,” Biomed. Opt. Express **5**(5), 1296–1308 (2014).
17. F. O. Fahrbach, V. Gurchenkov, K. Alessandri, P. Nassoy, and A. Rohrbach, “Light-sheet microscopy in thick media using scanned Bessel beams and two-photon fluorescence excitation,” Opt. Express **21**(11), 13824–13839 (2013).
18. T. A. Planchon, L. Gao, D. E. Milkie, M. W. Davidson, J. A. Galbraith, C. G. Galbraith, and E. Betzig, “Rapid three-dimensional isotropic imaging of living cells using Bessel beam plane illumination,” Nat. Methods **8**(5), 417–423 (2011).
19. C. Dunsby, “Optically sectioned imaging by oblique plane microscopy,” Opt. Express **16**(25), 20306–20316 (2008).
20. E. Sapoznik, B.-J. Chang, J. Huh, R. J. Ju, E. V. Azarova, T. Pohlkamp, E. S. Welf, D. Broadbent, A. F. Carisey, S. J. Stehbens, K.-M. Lee, A. Marín, A. B. Hanker, J. C. Schmidt, C. L. Arteaga, B. Yang, Y. Kobayashi, P. R. Tata, R. Kruithoff, K. Doubrovinski, D. P. Shepherd, A. Millett-Sikking, A. G. York, K. M. Dean, and R. P. Fiolka, “A versatile oblique plane microscope for large-scale and high-resolution imaging of subcellular dynamics,” eLife **9**, e57681 (2020).
21. M. B. Bouchard, V. Voleti, C. S. Mendes, C. Lacefield, W. B. Grueber, R. S. Mann, R. M. Bruno, and E. M. C. Hillman, “Swept confocally-aligned planar excitation (SCAPE) microscopy for high-speed volumetric imaging of behaving organisms,” Nat. Photonics **9**(2), 113–119 (2015).
22. M. Kumar, S. Kishore, J. Nasenbeny, D. L. McLean, and Y. Kozorovitskiy, “Integrated one- and two-photon scanned oblique plane illumination (SOPi) microscopy for rapid volumetric imaging,” Opt. Express **26**(10), 13027–13041 (2018).
23. M. Kumar and Y. Kozorovitskiy, “Tilt-invariant scanned oblique plane illumination microscopy for large-scale volumetric imaging,” Opt. Lett. **44**(7), 1706–1709 (2019).
24. B. Yang, X. Chen, Y. Wang, S. Feng, V. Pessino, N. Stuurman, N. H. Cho, K. W. Cheng, S. J. Lord, L. Xu, D. Xie, R. D. Mullins, M. D. Leonetti, and B. Huang, “Epi-illumination SPIM for volumetric imaging with high spatial-temporal resolution,” Nat. Methods **16**(6), 501–504 (2019).
25. F. O. Fahrbach, F. F. Voigt, B. Schmid, F. Helmchen, and J. Huisken, “Rapid 3D light-sheet microscopy with a tunable lens,” Opt. Express **21**(18), 21010–21026 (2013).
26. D. Xu, J. Ding, and L. Peng, “Structured illumination imaging with quasi periodic patterns,” J. Biophotonics **13**(6), e201960209 (2020).
27. K. Dholakia, N. Emptage, P. Haslehurst, and Z. Yang, “Fast volume-scanning light sheet microscopy reveals transient neuronal events,” Biomed. Opt. Express **9**(5), 2154–2167 (2018).
28. W. J. Shain, N. A. Vickers, B. B. Goldberg, T. Bifano, and J. Mertz, “Extended depth-of-field microscopy with a high-speed deformable mirror,” Opt. Lett. **42**(5), 995–998 (2017).
29. M. Duocastella, G. Sancataldo, P. Saggau, P. Ramoino, P. Bianchini, and A. Diaspro, “Fast inertia-free volumetric light-sheet microscope,” ACS Photonics **4**(7), 1797–1804 (2017).